Frequency and Parameter Combined Tuning Method of LCC-LCC Compensated Resonant Converter with Wide Coupling Variation for EV Wireless Charger

Junjun Deng, *Member, IEEE,* Qianning Mao, Wenbo Wang, Lantian Li, Zhenpo Wang, Shuo Wang, *Member, IEEE,* Giuseppe Guidi, *Senior Member, IEEE*

***Abstract*—The characteristics of inductive power transfer (IPT) systems are sensitive to the variation of the coupling coefficient caused by misalignment conditions or different gaps. This results in a reduction in transferred power and efficiency. The output characteristics considering frequency modulation applied in SS, LCC-S， and LCC-LCC compensated IPT systems have been explored, revealing that high order compensation topologies hold limited power regulation ability if coupling varies significantly. The parameter sensitivity of LCC-LCC compensated topology is investigated through the Singular Values (SVs) analysis. It is found that the variation of the parallel compensated capacitors have the greatest impact on the output power. Aiming at alleviating the power drop caused by the coupling variation, a parameter offline tuning method realized by switching the parallel compensated capacitance for a detuned LCC-LCC resonant converter is proposed for EV wireless charging. Analytical expressions have been derived in aiding the design of modified value of capacitance ensuring primary Zero Voltage Switching (ZVS) operation. Thus, the detuned parameter combinations, which deliver rated power even with the worst coupling, are obtained. Finally, a 6.6 kw prototype has been built to verify the validity of the proposed topology, which can deliver 6.1 kW with an efficiency of 94% even when the coupling drops from 0.3 to 0.15.**

***Index Terms*—anti-misalignment, detuned resonant tank, LCC-LCC compensation, Electric Vehicle (EV), frequency tuning method.**

NOMENCLATURE

$\mathbf{U}_{AB}$	Phasor of the first-order input voltage applied on the primary side.
U_{AB}	First-order rms value of the input voltage applied on the primary side.
$\mathbf{U}_{AB\_nth}$	Phasor of the *n*th-order input voltage.
U_{AB_nth}	The rms value of the *n*th-order input voltage.
u_{AB}	The square-wave input voltage applied on the primary side.
$\mathbf{U}_{ab}$	Phasor of the first-order output voltage before the rectifier.
U_{ab}	First-order rms value of the output voltage before the rectifier.
$\mathbf{I}_{Lf1}$	Phasor of the current on the primary-side compensation inductor L_{f1}.
I_{Lf1}	The rms value of the current on the L_{f1}.
I_{Lf1_nth}	The rms value of the *n*th-order input current.
$\mathbf{I}_1$	Phasor of the current on the transmitting coil L_1.
$\mathbf{I}_2$	Phasor of the current on the receiving coil L_2.
I_2	The rms value of the current on the receiving coil.
$\mathbf{I}_{Lf2}$	Phasor of the current on the secondary-side compensation inductor L_{f2}.
I_{Lf2}	The rms value of the current on the L_{f2}.
I_{off}	Turn-off current of the MOSFET.

I. Introduction

WIRELESS power transfer (WPT) technology can transfer energy from a power source to a load through electromagnetic fields or electromagnetic waves without electrical contact. Compared with the wired transmission method, WPT system has the advantages of safety, durability, and convenience. Thus, it is extensively studied for many applications, such as biomedical implants [1], mobile phones [2], trains [3], and especially electric vehicles (EVs) [4].

Inductive power transfer (IPT) has received the most attention for its relatively high power transfer capability and efficiency among WPT technologies applied in EVs [5]. The transmission of energy relies on loosely coupled coils. However, for stationary charged EVs, the inevitable misalignment between the coupling coils results in an increase in leakage inductance and a low coupling coefficient *k*, which deteriorates the system performance. To mitigate this problem, several

Manuscript received January 20, 2021; revised Feb 11, 2021; accepted Apr 10, 2021. (Corresponding author: Shuo.Wang@bit.edu.cn)

This work was partly supported by the National Key Research and Development Program of China (No. 2019YFE0104700), and partly supported by "Research and Demonstration of Key Technologies for Reliable and Efficient Application of New Energy Vehicles in China and Norway", funded by the Research Council of Norway under the China-Norway collaboration program, with project number 304213

J. Deng, Q. Mao, W. Wang, L. Li, Z. Wang, and S. Wang are all with the National Engineering Laboratory for Electric Vehicles, at Beijing Institute of Technology, Beijing 100081, China (e-mail: dengjunjun@bit.edu.cn; maoqianning@bit.edu.cn;wang_wenbo20@163.com; ericlee0126@gmail.com; wangzhenpo@bit.edu.cn; shuo.wang@bit.edu.cn).

Giuseppe Guidi is with the Electric Power System Department, SINTEF Energy Research, Sem Sælands vei 117034 Trondheim (e-mail: Giuseppe.Guidi@sintef.no).

This is the author accepted version of an article published in IEEE Journal of Emerging and Selected Topics in Power Electronics
https://doi.org/10.1109/JESTPE.2021.3077459

different approaches have been proposed. Some technologies that use video, sensors, and coils to reduce the deviation of parking positions have been developed [6]. However, these methods require additional equipment to guide parking, which increases cost and complexity. Redundant optimization of WPT systems which considers six degree of freedom (6DoF) misalignment tolerances simultaneously with high performance is investigated in [7]. Meanwhile, more efforts have been poured into the optimization of key components, which revolves around magnetic coupling devices, compensation topologies, and control strategies. A straightforward method is to optimize the magnetic coupler. Coil structures such as DD, DDQ, BP [8], and tripolar pads [9] enhance the anti-misalignment capability of the coupling coils in one or more directions by increasing the uniform magnetic field area. And the optimization process of coils parameters is further proposed [10]. In addition, asymmetric coil sets have significantly larger misalignment tolerance, the pick-up coil set is much smaller than the supply coil set in [11]. A structure with multiple transmitting coils or receiving coils is also presented [12]. However, it is necessary to analyze the cooperative work of multiple coils. And the interaction between the coils will also increase the difficulty of design. Recently, research on novel coil forms such as orthogonal winding [13] and three-phase systems [14] have expanded the system's tolerance for angular deviation.

On the other hand, many control strategies have been proposed to offset the impact of the coupling variation. Voltage tuning injected into the resonant tank, which can be achieved by regulating input voltage or the legs' phase shift of the inverter has been widely used [15]. To adjust the input voltage, a front-end DC-DC converter is usually introduced with duty cycle control. But it will increase the cost of the system, and the dynamic response of the cascaded stages is relatively slow. The phase-shifted method actively modulates the phase difference of the inverter's leg, which does not require additional circuits and has a good dynamic response. However, the phase-shifted range is limited by the soft-switching consideration which has an impact on the system efficiency. Frequency tuning is another widely used method to control the output power without additional conversion stages [15][16]. Since the impedance of the resonant components varies, the characteristics of the resonant network are affected. In [16], the regulation ability of frequency tuning on output performance has been investigated by simulation. The reflected impedance of the WPT circuit varies with the fluctuation of the coupling coefficient, resulting in the shift of resonant frequency. A lot of research has been carried out on frequency tracking, aiming at maintaining the resonance to ensure high efficiency [17][18]. However, the modeling of the detuned state is complicated, especially for high-order systems. Besides, the industry standards such as SAE J2954 [19] have constrained the operation frequency range, which limits the power regulation ability.

The design of the compensation topology also plays a key role in improving misalignment tolerance. A complicated hybrid compensation network that composes LCL and CL is reported in [20]. The proposed system maintains the output power within ±5% of its rated power when the coupling coefficient varies from 0.15 to 0.35. However, cross-coupling between components greatly increases the complexity of analysis. Thus, optimizing existing topologies is preferred, and some research focuses on the detuning design of topological parameters. As the most widely used topology, SS has been investigated for a detuned method [21], which expands the effective charging area by tuning the primary inductor and the secondary compensated capacitor to a slightly detuned state. However, in order to obtain a stable power, the efficiency is sacrificed. A detuned parameters design method for LCC-SP topology has been proposed in [22], in which the output current fluctuates less than 10% when the coupling coefficient changes from 0.2 to 0.5. Meanwhile, the LCC-LCC compensation topology with 8 components has more flexibility in parameter design for better misalignment tolerance [23]. However, the capability of the detuned method which adjusting the compensated parameters to improve the misalignment performance has not been investigated thoroughly.

This paper presents the modeling of frequency tuning characteristics of three commonly used topologies, including SS, LCC-S, and LCC-LCC. Analytical expressions of output power relating to frequency, coupling coefficient, and other parameters are derived with the same coupler. A quality factor is induced to quantify the load range related to the resonant impedance of the mesh containing the load, which provides better insight for compensation parameter design. Then the LCC-LCC topology is employed and investigated since its power regulation surface is monotonous. A sensitivity analysis is introduced to identify the most sensitive compensation component affecting the characteristic of LCC-LCC networks. Subsequently, the parameter design method is presented, in which the resonant converter can be switched between resonance and the detuned state. The detuned state is achieved by switching the values of the most sensitive components together with the operating frequency in an offline way for stationary EV charging, which holds the ability to maintain the rated output power even when the coupling drops to half of its original value.

The rest of the paper is organized as follows. The modeling and theoretical analysis of different compensation topologies are mentioned in Section II. The sensitivity analysis of LCC-LCC topology is introduced in Section III. In section IV, the design procedure of the proposed detuned method is presented considering the coupling variation and soft switching. In section V, the simulated results and the experimental results of a prototype are presented to validate the proposed method. Finally, Section VI concludes this paper.

II. Analysis Of Frequency Tuning Characteristics

The frequency ranges from 81.38-90 kHz according to SAE J2954 for EV wireless chargers [19]. And the characteristics of frequency tuning of different topologies should be evaluated within this limited adjustment range for their potential in resisting the power drop caused by the coupler misalignment.

There are three factors we have considered in selecting the topologies for EV charging applications. First, the voltage-fed

This is the author accepted version of an article published in IEEE Journal of Emerging and Selected Topics in Power Electronics
https://doi.org/10.1109/JESTPE.2021.3077459

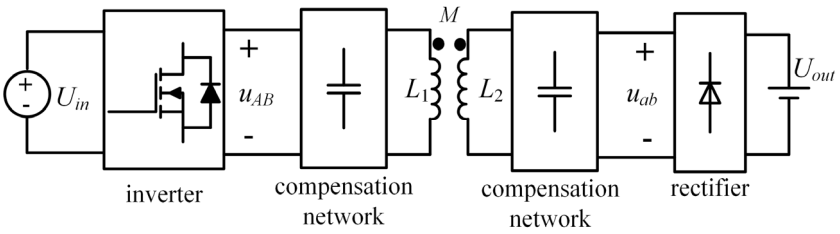

Fig. 1. A typical two-coil WPT system.

TABLE I
SPECIFICATION OF SS, LCC-S, LCC-LCC TOPOLOGIES

Topology	Var.	Description	Design value
Loosely coupled transformer	P_{out0}	Rated output power	6.6kW
	U_{in}	Input DC voltage	400V
	U_{out}	Output load voltage	250V-363V
	f_0	Resonate frequency	85kHz
	k_0	Rated coupling coefficient	0.3
	k	coupling coefficient	0.15-0.3
	R	Resistive load	9.5Ω-20Ω
	R_{eq}	Equivalent AC load	7.7Ω-16.2Ω
	L_1	Self-inductance of primary side	101.18μH
	L_2	Self-inductance of secondary side	101.18μH
SS	C_1	Series compensation capacitor of primary side	34.65nF
	C_2	Series compensation capacitor of secondary side	34.65nF
LCC-S	L_{f1}	Compensation inductance of primary side	33.45μH
	C_{f1}	Parallel compensation capacitor of primary side	105nF
	C_1	Series compensation capacitor of primary side	51.8nF
	C_2	Series compensation capacitor of secondary side	37.1nF
Doubled-sided LCC	L_{f1}	Compensation inductance of primary side	31.84μH
	L_{f2}	Compensation inductance of secondary side	31.84μH
	C_{f1}	Parallel compensation capacitor of primary side	110nF
	C_{f2}	Parallel compensation capacitor of secondary side	110nF
	C_1	Series compensation capacitor of primary side	50.6nF
	C_2	Series compensation capacitor of secondary side	50.6nF

inverters are more readily accessible. Therefore, the voltage-driven compensation networks are preferable, which refers to the SS and SP topology among the single capacitor compensation on each side. However, for SP compensation, the required primary compensated capacitance not only relates to the operating frequency but also the coupling coefficient, which is not preferred for soft-switching design. In this sense, the SS topology is preferable for simplicity. Second, for multi-component compensation topologies, the most complicated LCC-LCC topology holds advantages in terms of robustness to the load and coupling variation, since the sinusoidal current injected into the primary coil highly depends on the inverter's input voltage. Last but not least, to simplify the onboard secondary side for EVs while maintaining a relatively stable exciting current through the primary coil, the LCC-S topology is worthy of consideration. Consequently, SS, LCC-S, and LCC-LCC networks are chosen to be analyzed.

A typical two-coil WPT system is shown in Fig.1. The system includes the inverter, the compensation networks, the transmitting coil, the receiving coil, and the rectifier with the load. The parameters of the system are defined in Table I. All three topologies are targeted for the same external conditions as follows. U_{in}=400V is the DC voltage of the inverter, U_{out} is the voltage across the load, whose value varies from 250V to 363V during the charging process. Both the primary and secondary networks resonate at the frequency f_0=85 kHz. The rated coupling coefficient of the aligned transmitting and receiving coils is k_0=0.3. Considering the practical misalignment, the coupling coefficient ranges from 0.15 to 0.3. It should be noted that the analysis of the three systems is based on constant output power P_{out}=6.6 kW. Therefore, during the charging process, the load resistance and the equivalent AC resistance R_{eq} will change accordingly. R_{eq} is the equivalent AC load converted from the actual load to the input of the rectifier. As shown in Table I, the same external parameters are specified.

It should be pointed out that for SS compensated IPT system, the inductance of coupling coils L_1 and L_2 are determined once the rated coupling coefficient and frequency are given in a specific application. In comparison, coils' inductance of LCC-S and LCC-LCC compensated systems can be adjusted according to the value of the series compensated inductor. The parameters of the transmission coils of the three systems are the same since the same coupler is used. The specific parameters of compensation networks are also listed in Table I.

Besides, for compensation topologies containing LCC network, the compensated inductance needs to be calculated according to the rated input and output voltage. For LCC-S compensation topology, it can be calculated as [24],

$$L_{f1} = \frac{U_{AB} k_0 \sqrt{L_1 L_2}}{U_{ab}} \tag{1}$$

For double-sided LCC compensation topology, it can be

This is the author accepted version of an article published in IEEE Journal of Emerging and Selected Topics in Power Electronics
https://doi.org/10.1109/JESTPE.2021.3077459

TABLE II
SPECIFICATIONS OF THE DEFINED PARAMETERS

	SS	LCC-S	LCC-LCC
Inductance parameters	$L_1=L_2=L$	$L_1=L_2=L$	$L_1=L_2=L$ $L_{f1}=L_{f2}=L_f$
Resonant frequency	$f_0=\frac{1}{2\pi\sqrt{L_1C_1}}=\frac{1}{2\pi\sqrt{L_2C_2}}=\frac{1}{2\pi\sqrt{LC}}$	$f_0=\frac{1}{2\pi\sqrt{L_2C_2}}=\frac{1}{2\pi\sqrt{(L_1-L_{f1})C_1}}=\frac{1}{2\pi\sqrt{L_{f1}C_{f1}}}$	$f_0=\frac{1}{2\pi\sqrt{(L_1-L_{f1})C_1}}=\frac{1}{2\pi\sqrt{L_{f1}C_{f1}}}=\frac{1}{2\pi\sqrt{(L_2-L_{f2})C_2}}=\frac{1}{2\pi\sqrt{L_{f2}C_{f2}}}$
Characteristic impedance	$Z_0=\sqrt{\frac{L_2}{C_2}}=\sqrt{\frac{L}{C}}=2\pi f_0L$	$Z_0=\sqrt{\frac{L_2}{C_2}}=2\pi f_0L$	$Z_0=\sqrt{\frac{L_{f2}}{C_{f2}}}=\sqrt{\frac{L_f}{C_f}}=2\pi f_0L_f$
Quality factor		$Q=\frac{Z_0}{R_{eq}}$	

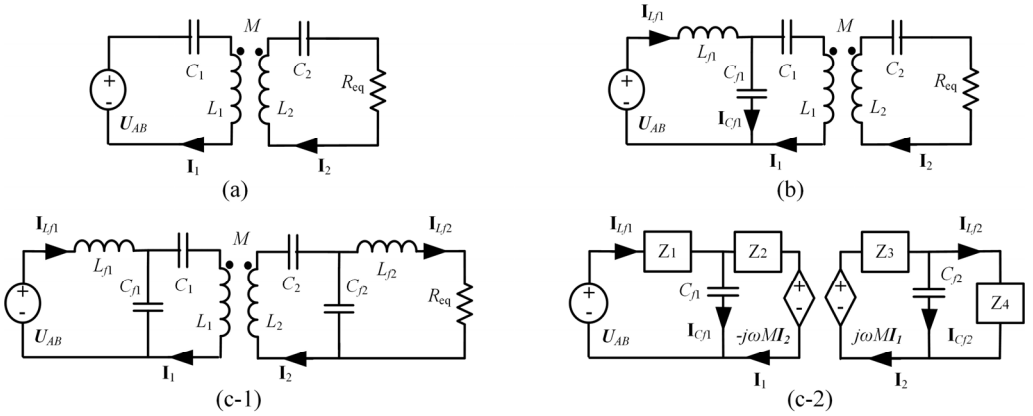

Fig. 2. Equivalent circuit with resistive load (a) SS topology; (b) LCC-S topology; (c) LCC-LCC topology.

calculated as [25],

$$L_{f1}=L_{f2}=\sqrt{\frac{U_{AB}U_{ab}k_0\sqrt{L_1L_2}}{P\omega_0}} \tag{2}$$

where P is the transferred power on the primary side. For simplicity, we take it as $P=P_{out0}$=6.6 kW without considering the loss.

Then the parameters of the corresponding compensation capacitors can be calculated according to the resonance frequency f_0.

In order to facilitate subsequent comparison and analysis, the following parameters are defined.

Normalized switching frequency f_n denotes the ratio of actual switching frequency to the resonance frequency,

$$f_n=\frac{f}{f_0}=\frac{2\pi f}{2\pi f_0}=\frac{\omega}{\omega_0} \tag{3}$$

Characteristic impedance Z_0,

$$Z_0=\sqrt{\frac{L}{C}} \tag{4}$$

Quality factor Q,

$$Q=\frac{Z_0}{R_{eq}}=\frac{1}{R_{eq}}\sqrt{\frac{L}{C}} \tag{5}$$

It should be pointed out that the above L and C refer to the inductance and capacitance elements contained in the mesh where the equivalent resistance is located. In the SS topology and the LCC-S topology, L and C refer to L_2 and C_2, respectively.

The characteristic impedance of SS topology and LCC-S topology is

$$Z_0(SS,LCC-S)=\sqrt{\frac{L_2}{C_2}}=2\pi f_0L_2=\frac{1}{2\pi f_0C_2} \tag{6}$$

As for LCC-LCC compensation topology, L_{f2} and C_{f2} are contained in the mesh with load, thus the characteristic impedance is

$$Z_0(LCC-LCC)=\sqrt{\frac{L_{f2}}{C_{f2}}}=2\pi f_0L_{f2}=\frac{1}{2\pi f_0C_{f2}} \tag{7}$$

The detailed information about f_n, Z_0, and Q of the three topological variables has been shown in Table II.

A. Analysis of the SS compensated IPT system

Fig.2(a) is the simplified resistive load circuits for the SS compensation network. The SS circuit described with Kirchoff's voltage law (KVL) is

This is the author accepted version of an article published in IEEE Journal of Emerging and Selected Topics in Power Electronics
https://doi.org/10.1109/JESTPE.2021.3077459

$$\begin{cases} \dfrac{1}{j\omega C_1}\mathbf{I}_1 + j\omega L_1\mathbf{I}_1 - j\omega M\mathbf{I}_2 - \mathbf{U}_{AB} = 0 \\ -j\omega M\mathbf{I}_1 + j\omega L_2\mathbf{I}_2 + \dfrac{1}{j\omega C_2}\mathbf{I}_2 + R_{eq}\mathbf{I}_2 = 0 \end{cases} \tag{8}$$

The expression of $\mathbf{I}_2$ with f_n, Q, and k is obtained,

$$\mathbf{I}_2 = \frac{jQf_n^3 k\mathbf{U}_{AB}}{L\omega_0(Qf_n^4(k^2-1)+2Qf_n^2+j(f_n^3-f_n)-Q)} \tag{9}$$

The power on the load can be calculated as

$$P_{out} = I_2^{\,2} R_{eq} \tag{10}$$

It can be seen from equation (9) that the output power expression of the SS resonant converter contains three independent variables. The coupling coefficient k varies with the misalignment of the coils. The operating switching frequency f and the quality factor Q represent the operating conditions of the converter. When a coupling coefficient k is given, the output performance can be obtained in the frequency domain with the change of the quality factor Q, which represents the variation of the equivalent load resistance R_{eq}. The normalized output power $P_n = P_{out}/P_{out0}$ for k=0.15, k=0.225 and k=0.3 within the frequency range 75-95 kHz is shown in Fig.3. The red line refers to P_n=1. It can be seen that the transfer power is sensitive to the variation of the coupling coefficient. The output power greatly increased as the coupling coefficient decreases. This situation requires additional control, otherwise the circuit may suffer from the overcurrent when the coupler is misaligned, which is disadvantageous for electronic devices. Besides, it can be observed that the frequency splitting phenomenon appears, which increases the difficulty of designing the frequency modulation strategy.

B. Analysis of the LCC-S compensated IPT system

Fig.2(b) is the simplified resistive load circuits for the LCC-S compensation network. The LCC-S circuit described with Kirchoff's voltage law (KVL) is

$$\begin{cases} -\mathbf{U}_{AB} + j\omega L_{f1}\mathbf{I}_{Lf1} + (\mathbf{I}_{Lf1} - \mathbf{I}_1)\dfrac{1}{j\omega C_{f1}} = 0 \\ -(\mathbf{I}_{Lf1} - \mathbf{I}_1)\dfrac{1}{j\omega C_{f1}} + \dfrac{1}{j\omega C_1}\mathbf{I}_1 + j\omega L_1\mathbf{I}_1 - j\omega M\mathbf{I}_2 = 0 \\ -j\omega M\mathbf{I}_1 + j\omega L_2\mathbf{I}_2 + \dfrac{1}{j\omega C_2}\mathbf{I}_2 + R_{eq}\mathbf{I}_2 = 0 \end{cases} \tag{11}$$

The expression of $\mathbf{I}_2$ with f_n, Q, and k is given by (12) shown at the bottom of this page.

Similarly, we can calculate the output power by substituting equation (12) into equation (10). Fig.4 shows the normalized output power P_n for k=0.15, k=0.225, and k=0.3 within the frequency range 80-90 kHz with the varying Q. Compared with SS topology, the output power surface of LCC-S topology tends to unimodal, and the peak value appears right at the resonance frequency. It means that the frequency modulation can be implemented in the way of increasing the frequency or decreasing the frequency started from the resonant frequency. In addition, it can be seen that the capability of transferring power decreases as the coupling coefficient drops. When the coupling coefficient drops to a certain level, rated power couldn't be guaranteed since the red line disappeared from the surface. It can be inferred from Fig.4 (a) that a higher quality factor Q can be a solution considering the low coupling coefficient. In this case, a larger inductance is needed if the load resistor is kept, which means more energy should be injected into the resonant tank. However, it also means an over-design at the rated coupling condition since the peak of the surface rises. That is to say, if the system is designed based on the worst case of coupling, it leads to an excess transmission capacity of the system, which is usually bulky and costly.

C. Analysis of the LCC-LCC compensated IPT system

Fig.2(c) is the simplified resistive load circuits for the LCC-LCC compensation network. The circuit in Fig.2(c-1) is further simplified to Fig.2(c-2), in which

$$\begin{cases} Z_1 = j\omega L_{f1} \\ Z_2 = \dfrac{1}{j\omega C_1} + j\omega L_1 \\ Z_3 = \dfrac{1}{j\omega C_2} + j\omega L_2 \\ Z_4 = j\omega L_{f2} + R_{eq} \\ Z_m = j\omega M \end{cases} \tag{13}$$

The LCC-LCC circuit described with Kirchoff's voltage law (KVL) is

$$\begin{cases} Z_1\mathbf{I}_{Lf1} + \dfrac{1}{j\omega C_{f1}}\mathbf{I}_{Cf1} - \mathbf{U}_{AB} = 0 \\ Z_2\mathbf{I}_1 - Z_m\mathbf{I}_2 - \dfrac{1}{j\omega C_{f1}}\mathbf{I}_{Cf1} = 0 \\ Z_3\mathbf{I}_2 + \dfrac{1}{j\omega C_{f2}}\mathbf{I}_{Cf2} - Z_m\mathbf{I}_3 = 0 \\ Z_4\mathbf{I}_{Lf2} - \dfrac{1}{j\omega C_{f2}}\mathbf{I}_{Cf2} = 0 \end{cases} \tag{14}$$

The expression of $\mathbf{I}_{Lf2}$ with f_n, Q, and k is given by (15) shown at the bottom of this page.

Substituting equation (15) into equation (10), replace I_2 with I_{Lf2}, the output power could be calculated. Fig.5 shows the normalized output power P_n for k=0.15, k=0.225, and k=0.3 within the frequency range 80-90 kHz as the quality factor Q varies. The output power surface of the LCC-LCC topology has

$$\mathbf{I}_2 = \frac{Qf_n^3 k\mathbf{U}_{AB}}{\omega_0\left[jQL\left[(k^2-1)f_n^6-(k^2-3)f_n^4\right]+jQ\left[-(3L-L_f)f_n^2+(L-L_f)\right]+L(-f_n^5+2f_n^3)+(L_f-L)f_n\right]} \tag{12}$$

$$\mathbf{I}_{Lf2} = \frac{Qf_n^3 kL\mathbf{U}_{AB}}{\omega_0\left[\left[k^2f_n^4-(f_n^2-1)^2\right]\left[jQ(f_n^2-1)^2+f_n(f_n^2-1)\right]L^2+\left[2jQ(f_n^2-1)^2+f_n(f_n^2-1)\right]LL_f-jL_f^{\,2}Q\right]} \tag{15}$$

This is the author accepted version of an article published in IEEE Journal of Emerging and Selected Topics in Power Electronics
https://doi.org/10.1109/JESTPE.2021.3077459

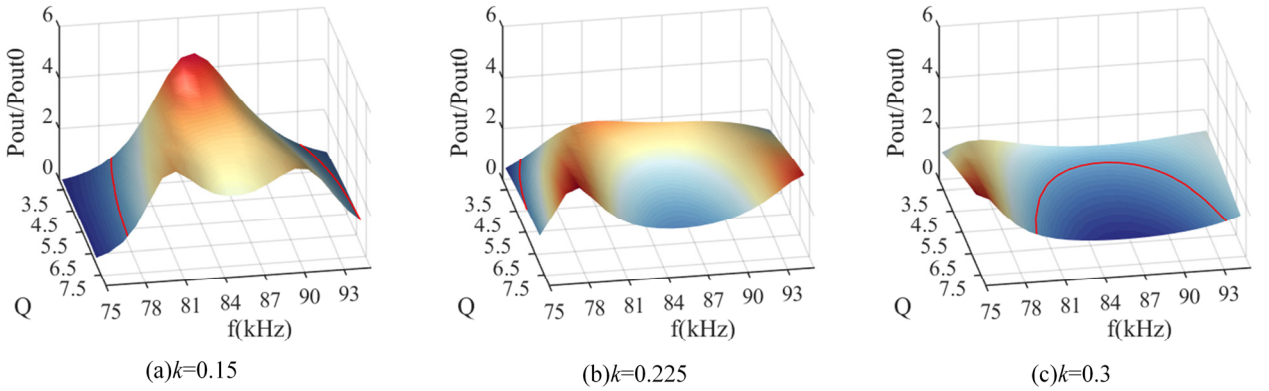

(a)k=0.15 (b)k=0.225 (c)k=0.3

Fig. 3 The normalized output power Pout/Pout0 of SS system

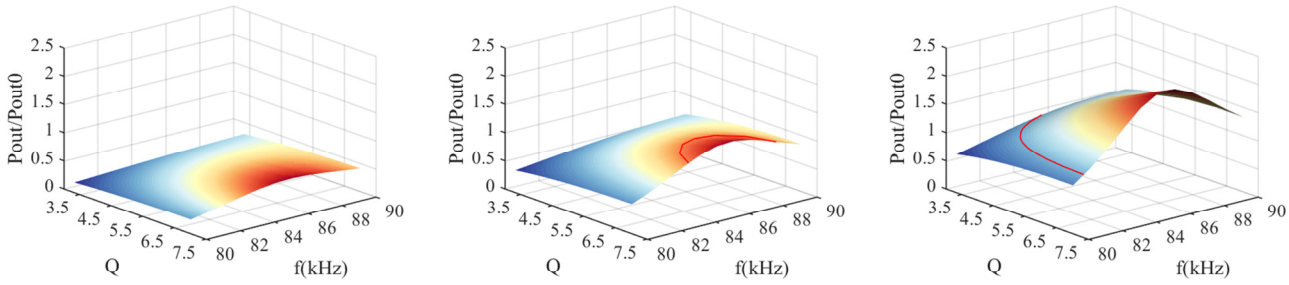

(a)k=0.15 (b)k=0.225 (c)k=0.3

Fig. 4 The normalized output power Pout/Pout0 of LCC-S system.

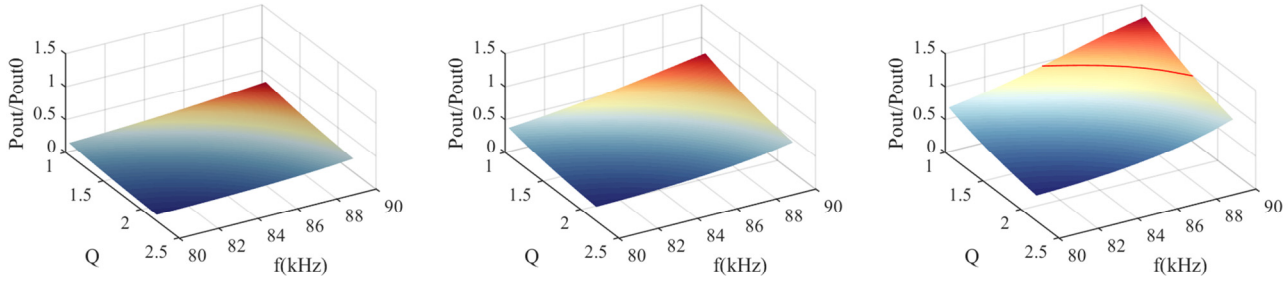

(a)k=0.15 (b)k=0.225 (c)k=0.3

Fig. 5 The normalized output power Pout/Pout0 of LCC-LCC system.

monotonicity. The transfer power increases monotonically with the increase of the frequency f as well as Q and k. For the SS topology, there is a frequency splitting region in the power surface, and it is uncertain whether the output power increases or decreases with the increase of the frequency. In Fig.5, there exists a range in which the frequency modulation fails when the coupling coefficient is small. It means the ability of the frequency tuning method is limited for LCC-LCC compensation. Specifically, for the system shown in Fig. 5, if the coupling coefficient $k < 0.225$, although the frequency is tuned to the upper limit, the desired output power could not be delivered. Again, designing under the worst-case conditions is a common but not optimal solution.

From the previous analysis, it is not practical to achieve the purpose of maintaining power stability merely through frequency tuning. It has been proved that parameter tuning can be an alternative method [21]. For topologies with few components like SS circuit, the available tuning components are clear and analysis is easier. However, complex topologies such as LCC-LCC compensation topology are different stories since more parameters are involved. Therefore, key parameters that can be tuned for power regulation should be identified first. Considering the LCC-LCC compensation topology has the highest degree of freedom, it is taken as an example to introduce the design process of the sensitive parameter detuning method.

As mentioned before, coupling coils' inductance of LCC-S and LCC-LCC compensated systems are not restricted by targeted specifications. One advantage of the LCC-LCC compensated IPT system is that it has more degrees of freedom in parameter design. In general, coils with larger inductance values are preferred. As for the same transferring power and coupling coefficient, the larger the inductance, the smaller the current flowing through the coils. It is undeniable that the increase in the inductance value leads to a larger coil with more

This is the author accepted version of an article published in IEEE Journal of Emerging and Selected Topics in Power Electronics
https://doi.org/10.1109/JESTPE.2021.3077459

Litz wires which increases the coil resistance. However, due to the square relationship between the loss and the current, the current has a greater impact on the loss than the resistance. The current decreases more and the resistance increases less with larger L_1 and L_2, the loss will be smaller, which helps to improve the efficiency of the system and reduce the current stress on the wiring harness. Taking into account the allowable installation size of the vehicle chassis and making a trade-off between the transmission efficiency and cost, the self-inductance of the LCC- LCC system is set to be 240μH in the following analysis.

III. Sensitivity Analysis

In [26], a general Singular Values (SVs) analysis method is proposed to investigate the impact of parameter variations on the system output performance. SVs method is applied in this paper to investigate the most sensitive parameters among LCC-LCC networks, including C_1, C_2, C_{f1}, C_{f2}, L_1, L_2, L_{f1}, and L_{f2}. The system shown in Fig.2(c-1) is modeled by 8 state variables, the voltage across capacitors and current through inductors.

$$\boldsymbol{x}=\left[\mathbf{U}_{C1}\quad \mathbf{U}_{Cf1}\quad \mathbf{U}_{C2}\quad \mathbf{U}_{Cf2}\quad \mathbf{I}_{1}\quad \mathbf{I}_{Lf1}\quad \mathbf{I}_{2}\quad \mathbf{I}_{Lf2}\right]^{T} \tag{16}$$

The input vector $\boldsymbol{u}$ and the output vector $\boldsymbol{y}$ are expressed as

$$\boldsymbol{u}=\left[\mathbf{U}_{AB}\quad \mathbf{U}_{ab}\right]^{\mathrm{T}} \tag{17}$$

$$\boldsymbol{y}=\left[\mathbf{I}_{1}\quad \mathbf{I}_{Lf2}\right]^{\mathrm{T}} \tag{18}$$

The state equation and the output equation are

$$\dot{\boldsymbol{x}}=\boldsymbol{A}\boldsymbol{x}+\boldsymbol{B}\boldsymbol{u} \tag{19}$$

$$\boldsymbol{y}=\boldsymbol{C}\boldsymbol{x} \tag{20}$$

In these formulas, $\boldsymbol{A}$, $\boldsymbol{B}$ and $\boldsymbol{C}$ are three matrixes containing the inductive and capacitive parameters of the system, and the details can be found in [26]. The transfer function $\boldsymbol{G}$ is calculated, which can represent the system.

$$\boldsymbol{G}(s)=\frac{\boldsymbol{Y}(s)}{\boldsymbol{U}(s)}=\boldsymbol{C}(s\boldsymbol{I}-\boldsymbol{A})^{-1}\boldsymbol{B} \tag{21}$$

$\boldsymbol{G}$ of the dynamic model is used to obtain SVs, σ of the system, which represents the gain of the system in the corresponding input direction. The maximum gain of the system is the largest SV $\bar{\sigma}$, while the minimum gain of the system is the smallest SV $\underline{\sigma}$, thus

$$\underline{\sigma}\le\frac{\left\|\boldsymbol{G}(j\omega)\boldsymbol{u}(j\omega)\right\|_2}{\left\|\boldsymbol{u}(j\omega)\right\|_2}\le\bar{\sigma} \tag{22}$$

The percentage change in maximum SV $\bar{\sigma}$ when inductances and capacitances deviate ±20% is calculated to investigate the sensitivity of the system to parameters.

$$\Delta\bar{\sigma}(\%)=\frac{\bar{\sigma}(\boldsymbol{G}')-\bar{\sigma}(\boldsymbol{G}_0)}{\bar{\sigma}(\boldsymbol{G}_0)}\times100\% \tag{23}$$

$\bar{\sigma}(\boldsymbol{G}_0)$ is the largest SV of the system with rated parameters, while $\bar{\sigma}(\boldsymbol{G}')$ is the largest SV when parameters are tuned. The results are plot in Fig.6. The larger the value is, the more sensitive the system will be. It is found that at a given frequency, $\bar{\sigma}$ and the output power is most sensitive to C_{f1}, C_{f2}, followed by L_2.

Based on the above analysis, one possible approach is

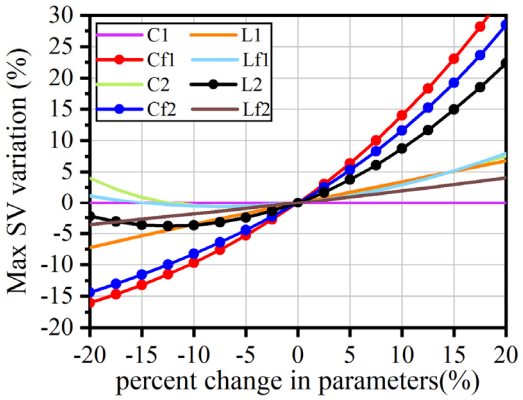

Fig. 6. Percentage change of maximum singular values with ±20% deviation for parameters.

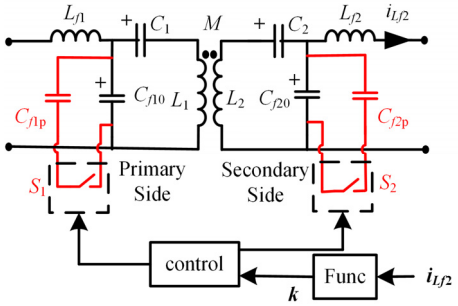

Fig. 7. Topology of detuned LCC-LCC compensated converter.

adjusting the value of the sensitive parameters such as C_{f1} and C_{f2} for a detuned state, in which the resonant tank's output characteristic is changed to offset the coupling drops together with frequency modulation. The proposed topology is shown in Fig.7. C_{f10} and C_{f20} represent capacitors with rated values in the resonance state. C_{f10} is connected in parallel with a capacitor C_{f1p}, controlled by a switch S_1. The same goes for C_{f2}.

S_1 and S_2 are controlled according to the detected coupling coefficient k. Assuming resonance is achieved with the rated operation frequency f=85 kHz, the coupling coefficient k can be calculated [25].

$$k=\frac{\pi}{2\sqrt{2}U_{in}}\cdot\frac{I_{Lf2}\omega_0 L_{f1}L_{f2}}{\sqrt{L_1L_2}} \tag{24}$$

Where U_{in}, I_{Lf2} can be measured by sensors. ω_0 is the resonant angular frequency. L_1, L_2, L_{f1}, and L_{f2} can be regarded as constants for a specific system, although variation can be observed for the coupler's self-inductance due to misalignment.

Then, the calculated coupling is compared to a designed threshold to determine if the backup parallel compensation capacitors C_{f1p} and C_{f2p} for tuning should be connected by closing the switches. For example, in this paper, when $k\le0.225$, the desired output power could not be delivered by regulating the operating frequency (81.38 kHz-90 kHz). And the switches S_1 and S_2 should be closed.

In the application of wireless charging for EVs, the coupling coils' misalignment is caused by the parking deviations. Once the car has been parked, the coupling is supposed to be fixed during the charging process unless foreign objects enter. In this

This is the author accepted version of an article published in IEEE Journal of Emerging and Selected Topics in Power Electronics
https://doi.org/10.1109/JESTPE.2021.3077459

case, the detection of the coupling coefficient and the switching of the capacitor are carried out in the initialization stage of the charging process.

When switches S_1 and S_2 are closed, C_{f10} and C_{f1p} can be regarded as a new compensation capacitor C_{f1}. Also, C_{f20} and C_{f2p} form a new compensation capacitor C_{f2}. We define

$$\begin{aligned} C_{f1} &= C_{f10} + C_{f1p} = \alpha C_{f10} \\ C_{f2} &= C_{f20} + C_{f2p} = \beta C_{f20} \end{aligned} \tag{25}$$

Note that α and β are the tuning weight coefficient of C_{f10} and C_{f20} respectively, which will be focused on in the following analysis.

IV. Design Procedure

Aiming at switching to a detuned state, two requirements should be considered.

1) As the coupling coefficient decreases due to the misalignment, C_{f1} and C_{f2} are switched from their resonant value.

2) To reduce the switching loss, the turn-off current of the MOSFET should be analyzed to ensure ZVS condition of another MOSFET in the same arm.

The detuned topology is analyzed numerically to determine the value of α and β. The performance is analyzed based on the system with resistive load presented in Figure 2(c). Substituting (25) into (14), the output current $\mathbf{I}_{Lf2}$ and the input current $\mathbf{I}_{Lf1}$ containing frequency f and α, β are expressed as

$$\begin{aligned} \mathbf{I}_{Lf2} &= \frac{-jZ_m \mathbf{U}_{AB}}{\boldsymbol{K}} \\ \mathbf{I}_{Lf1} &= \frac{-\mathbf{U}_{AB}\left(C_{f10}\alpha\omega \cdot \boldsymbol{K} - jC_{f20}Z_3Z_4\beta\omega - Z_3 - Z_4\right)}{\boldsymbol{K}\cdot\left(-C_{f10}Z_1\alpha\omega + j\right)} \end{aligned} \tag{26}$$

Where

$$\begin{aligned} \boldsymbol{K} &= j\left(C_{f10}C_{f20}Z_1Z_4K_1\alpha\beta\omega^2 - K_4\right) \\ &\quad + \left(C_{f10}Z_1K_3\alpha\omega + C_{f20}Z_4K_2\beta\omega\right) \\ K_1 &= Z_2Z_3 - Z_m{}^2 \\ K_2 &= Z_1Z_3 + K_1 \\ K_3 &= Z_2Z_4 + K_1 \\ K_4 &= Z_1Z_3 + Z_1Z_4 + K_3 \end{aligned} \tag{27}$$

A. Output Power

Using Equation (10), whether the output power meets the requirement could be calculated from I_{Lf2}. Thus, I_{Lf2} is investigated instead of the power since the current can be measured directly. In this paper, it should be noted that k=0.15 is chosen to represent the worst case, and the switching frequency 89 kHz is chosen since it is the maximum frequency specified by the standard.

$\mathbf{U}_{AB}$ is the phasor of the first-order input voltage and its phase angle is 0°. Take $\mathbf{U}_{AB}$ as the reference for other voltages and currents. We have

$$\mathbf{U}_{AB} = U_{AB}\angle 0^\circ = \frac{1}{\sqrt{2}}\frac{4}{\pi}U_{\text{in}} \tag{28}$$

U_{in} is the input DC voltage of the inverter. Substituting Equation (28) into Equation (26), the fundamental output current $\mathbf{I}_{Lf2}$ can be derived. The amplitude of $\mathbf{I}_{Lf2}$ is I_{Lf2}, and I_{Lf2} is the rms value of the current through the equivalent resistive load R_{eq}. Fig.8(a) is the graph of I_{Lf2} with α and β variated between 100%-150% at 89 kHz when k=0.15. The rated value of I_{Lf2} is calculated as 19.8A, as shown by the dashed line. In this paper, we stipulate that an error of ±10% is allowed. Then, considering ±10% tolerance, 17.8A and 21.8A are accepted as the lower boundary and upper boundary respectively, as the two solid lines shown in Fig.8. The corresponding vertical view is shown in Fig.8(b). And the region between the two boundaries could meet the output power. Thus, a series of α and β combinations that can achieve rated power are initially obtained.

B. ZVS

Reducing the switching loss of the MOSFET could be achieved with ZVS [27]. The output current should lag its output voltage for a full-bridge inverter, that is, the input impedance Z_{in} of the load network should be inductive. In other words, the phase angle θ_{in} of Z_{in} is required to be slightly larger than zero, θ_{in}>0°.

The input impedance is calculated

$$\begin{aligned} Z_S &= Z_4 \,\|\, \frac{1}{j\omega C'_{f2}} + Z_3 \\ Z_f &= \frac{\omega^2 M^2}{Z_S} \\ Z_{in} &= \left(Z_f + Z_2\right) \| \frac{1}{j\omega C'_{f1}} + Z_1 \end{aligned} \tag{29}$$

From Z_{in} in (29), the input phase angle is calculated as

$$\theta_{in} = \frac{180}{\pi}\tan^{-1}\frac{\text{Im}(Z_{in})}{\text{Re}(Z_{in})} \tag{30}$$

Fig.9 is the graph of θ_{in} with α and β variated from 100% to 150% at 89 kHz when k=0.15. The red line corresponds to the cases that the phase angle of the input impedance is 0°, which is regarded as the zero phase angle (ZPA) boundary between the inductive region and the capacitive region. Specifically, the region on the right side of the ZPA boundary is the inductive region, in which we have θ_{in}>0°. It can be seen that Z_{in} is more inductive as C_{f1} and C_{f2} deviate further. In contrast, the left side of the boundary means the capacitive cases with θ_{in}<0°.

The turn-off current of the MOSFET should be controlled more precisely to keep a reasonable VA rating. The turn-off current should meet:

$$I_{off} \geq \frac{4C_{oss}V_{in,\max}}{t_d} = 1.34\text{A} \tag{31}$$

Where, C_{oss} is the output capacitance of the MOSFET, and C_{oss}=C_{ds}+C_{gd}. t_d is the dead time. That is to say, the minimum turn-off current that ZVS can be achieved is 1.34A in theory.

To ensure the value of the calculated turn-off current is accurate, the higher harmonics of the square wave voltage u_{AB} need to be taken into consideration. The square-wave voltage at the output of the inverter is expressed as

$$u_{AB}(t) = \frac{4}{\pi}\mathbf{U}_{in}\sum_{n=1,3,5\ldots}^{\infty}\frac{\sin(n\omega t)}{n} \tag{32}$$

This is the author accepted version of an article published in IEEE Journal of Emerging and Selected Topics in Power Electronics
https://doi.org/10.1109/JESTPE.2021.3077459

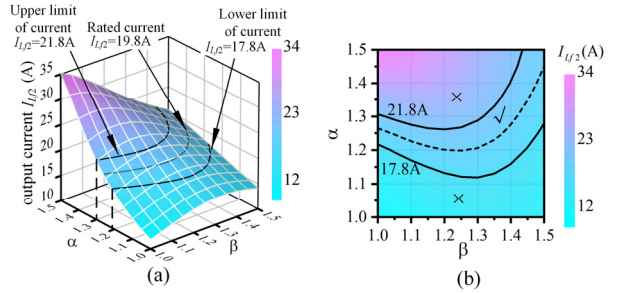

Fig. 8. α and β variated 100%-150%, k=0.15, f=89 kHz (a)I_{Lf2} in 3D graphics; (b) the corresponding vertical view of I_{Lf2}

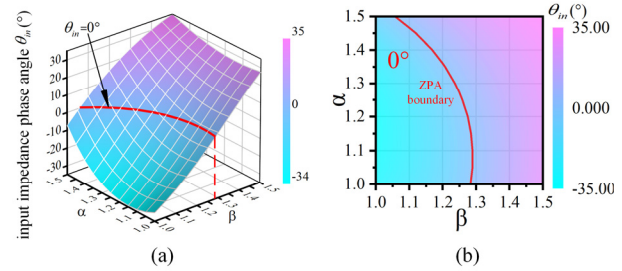

Fig. 9. α and β variated 100%-150%, k=0.15, f=89 kHz (a) θ_{in} in 3D graphics; (b) the corresponding vertical view of θ_{in}.

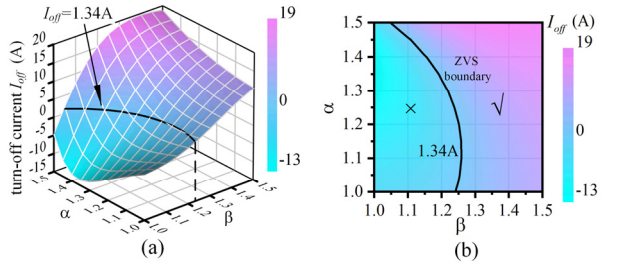

Fig. 10. α and β variated 100%-150%, k=0.15, f=89 kHz (a) I_{off} in 3D graphics; (b) the corresponding vertical view of I_{off}.

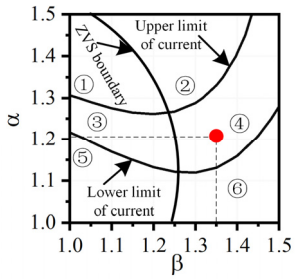

Fig. 11. The plane divided by the current boundary and ZVS boundary.

The rms value of the nth harmonic can be expressed as

$$U_{AB\_nth} = \frac{1}{\sqrt{2}} \frac{4}{\pi} \frac{U_{in}}{n} \tag{33}$$

The frequency of the nth harmonic is

$$\omega_{n\_th} = n\omega \tag{34}$$

The nth current I_{Lf1_nth} can be obtained by substituting Equation (33) and (34) into Equation (26). Replace U_{AB} and ω in (26) with U_{AB_nth} and ω_{n_th} respectively.

Similarly, the corresponding input impedance angle θ_{in_nth} is derived by substituting Equation (34) into Equation (29), and then substituting Equation (29) into Equation (30). Replace ω in (29) with ω_{n_th}, then the phase angle θ_{in_nth} corresponding to the nth current can be calculated.

At the turn-off moment t=0, the turn-off current I_{off} is the sum of the fundamental value and other harmonics values,

$$I_{\substack{off \\ t=0}} = \sqrt{2}(I_{Lf1\_1} \cdot \sin\theta_{in\_1} + I_{Lf1\_3} \cdot \sin\theta_{in\_3} + \ldots + I_{Lf1\_n} \cdot \sin\theta_{in\_n}) \tag{35}$$

Calculated results of I_{off} with α and β variated 100%-150% at 89 kHz are shown in Fig.10(a). The black line is the minimum current to discharge the junction capacitor in theory, I_{off}=1.34A, which is the ZVS boundary. And the corresponding vertical view is shown in Fig.10(b). The right part of the ZVS boundary can meet the requirements of the soft switching theoretically.

It is to be noted that in calculating the phase angle of the input impedance, only the first harmonic has been considered to plot the ZPA boundary. While obtaining the ZVS boundary, the high-order harmonics have been taken into consideration since they will have an impact on the turn-off current, especially in detuned conditions. Therefore, operating in the inductive region indicated by the ZPA boundary is a necessary condition for realizing soft-switching, while operating in the ZVS region indicated by the ZVS boundary is a feasible condition since it can be designed according to the MOSFETs' parasitic parameters.

C. *Considerations*

α and β are further selected among combinations obtained in the previous step. As shown in Fig.11, it has been divided into 6 regions by upper limit of current, lower limit of current, and the ZVS boundary. Specifically, region 3 and region 4 meet the power requirements, while the region 2, 4, and 6 can ensure the ZVS. All in all, region 4 is the preferred area, in which combinations of α and β meet both power requirements and ZVS requirements.

The following factors should be considered when choosing α and β. On the one hand, α and β should be as small as possible. Large values of α and β mean the regulated detuned state is farther away from the rated resonance, which causes a larger reactive power in the resonant tank. Besides, it also means more capacitors should be adopted, which increases the cost.

On the other hand, a certain margin is needed to ensure the realization of ZVS in practice. Because errors exist in using the value from the MOSFETs' datasheet as the actual parasitic capacitance. Therefore, the targeted turn-off current should be designed to be slightly larger than the theoretical value.

Finally, α=1.2 and β=1.35 shown in Fig.11 are chosen since it is the combination with relatively small α and β in the region 4, which corresponds to I_{Lf2}=19.24A and I_{off}=5.1A.

The implementation process is concluded below.

1) Obtain the rated parameters of the system.

2) The most sensitive parameters are found to be C_{f1} and C_{f2} through sensitivity analysis.

3) In practice, when the coupling coils are shifted, obtain the actual coupling coefficient k.

4) Compare the actual coupling coefficient k with the designed threshold.

5) If the frequency tuning method fails, change α and β to select the combinations that required power is achievable.

This is the author accepted version of an article published in IEEE Journal of Emerging and Selected Topics in Power Electronics
https://doi.org/10.1109/JESTPE.2021.3077459

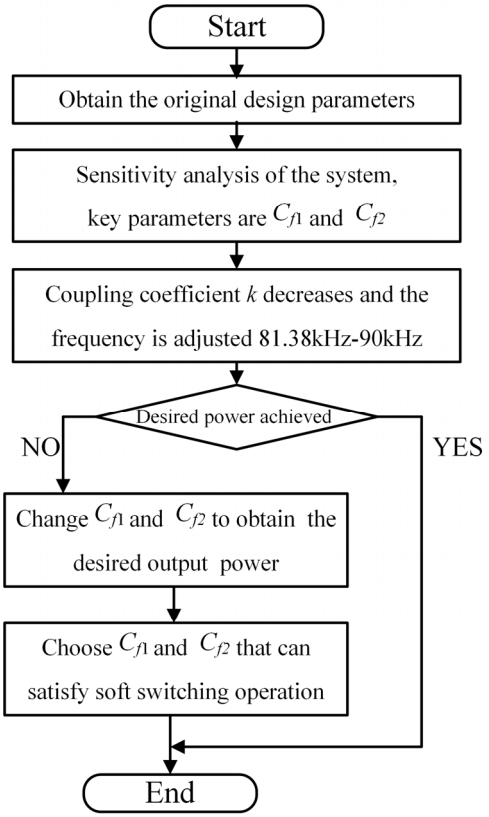

Fig. 12. Flowchart of the design.

6) The pairs of the solution obtained in step (5) are substituted into Equation (35) to calculate the current through MOSFET at the turn-off moment. The pairs that can achieve ZVS with minimum variation are picked.

The flowchart is shown in Fig.12.

V. Simulation And Experiments Results

The feasibility of the proposed parameter tuning method is verified through the simulation and the experiment. The designed and measured circuit parameters are listed in Table III. The coupling coefficient is controlled by changing the distance between the aligned coupling coils.

As for simulation, a 6.6 kW model is established in LTspice to simulate the output performance of the system. In two cases, coupling coefficient k=0.3 with frequency f=85 kHz is simulated to represent the standard condition, and k=0.15, f=89 kHz with α=1.2 and β=1.35 is simulated as the worst case. The simulated results of the output current I_{Lf2} and the switch current I_{off} for different α and β are shown in Fig.13. Compared with the calculated results, the theoretical analysis is validated. The simulated waveforms for two conditions are shown in Fig.14. Similar waveforms of these two conditions can be achieved, and ZVS for MOSFETs is realized in the worst condition.

A 6.6 kW prototype is tested to verify its practical feasibility. The coupling coils are symmetrical DD-type, and each rectangular coil is wounded with 10 turns of Litz wire in a single layer. The size of the coupler is 500mm*550mm. By simulating in Maxwell, when the gap between the coupling coils varies from 148mm to 230mm, the coupling coefficients drop from 0.3 to 0.15, which has been validated experimentally.

TABLE III
Specifications Of The Experimental IPT System

Var.	Design value	Measurement
U_{in}	400V	400V
U_{out}	363V	363V
L_1	240μH	244.5μH/234.9μH
L_2	236μH	239.6μH/231.1μH
L_{f1}	49μH	48.9μH
L_{f2}	50μH	51.3μH
C_1	18.36nF	18.44nF
C_2	18.85nF	18.86nF
C_{f1}	71.5nF/85.8nF	71.56nF/86.1nF
C_{f2}	70.1nF/94.635nF	69.75nF/94.7nF
f	85kHz/89kHz	85kHz/89kHz
/	148mm/230mm	134mm/215mm
k	0.3/0.15	0.3/0.15
R	20.52Ω	20.52Ω

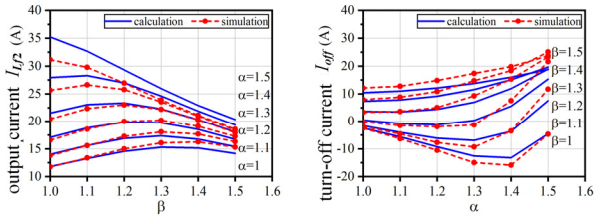

Fig. 13. Simulation and theoretical calculation of the detuned system, f=89 kHz, k=0.15 (a) I_{Lf2} (b) Turn-off current I_{off}.

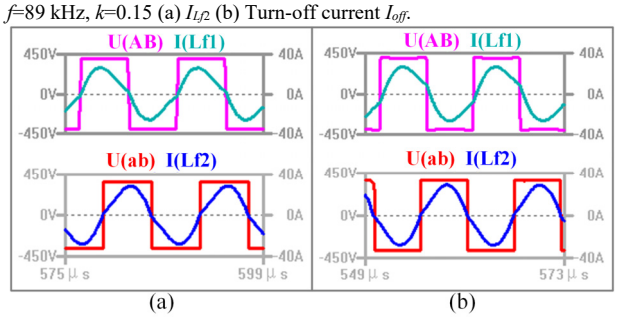

Fig. 14. Simulation waveform of $\mathbf{U}_{AB}$, $\mathbf{I}_{Lf1}$, $\mathbf{U}_{ab}$, $\mathbf{I}_{Lf2}$ (a) k=0.3, f=85 kHz (b) k=0.15, f=89 kHz.

Fig.15 shows the experimental setup. The full-bridge inverter's MOSFETs model is C2M0080120D, which operates at 80-89 kHz. Rectifier diodes are DSEI120-06A. The output filter capacitor is 10μF. The load is composed of a group of resistors in series and parallel. The voltage and current are measured by LV-25P voltage sensor and HO 25-P/SP33 current sensor respectively. YOKOGAWA WT1800 Power Analyzer is used to analyze the transfer power and efficiency. Tektronix TBS 2000 is used to observe the waveform.

Fig.16 illustrates the steady waveforms of the primary side and the secondary side. Fig.16(a) corresponds to the standard condition used as a reference, and Fig.16(b) is the worst case when k=0.15 with the detuned LCC-LCC compensation parameters. Similar waveforms are obtained. In Fig.16(b), it should be noted that the normally undesired detuned states, which lead to larger reactive power in the resonant tank, are used to deal with the coupling drops. The operating frequency as well as the values of the compensated components are both

This is the author accepted version of an article published in IEEE Journal of Emerging and Selected Topics in Power Electronics
https://doi.org/10.1109/JESTPE.2021.3077459

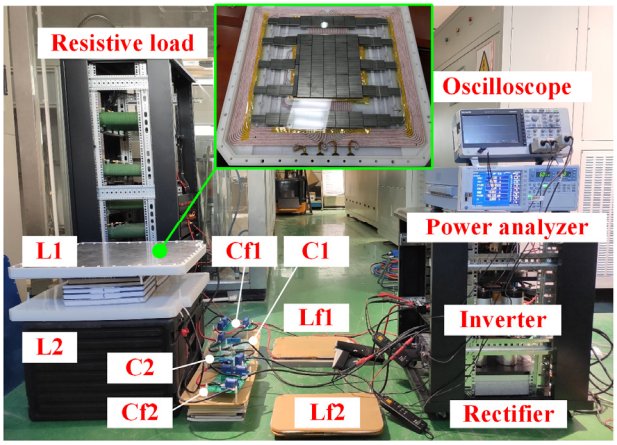

Fig. 15. Experiment setup

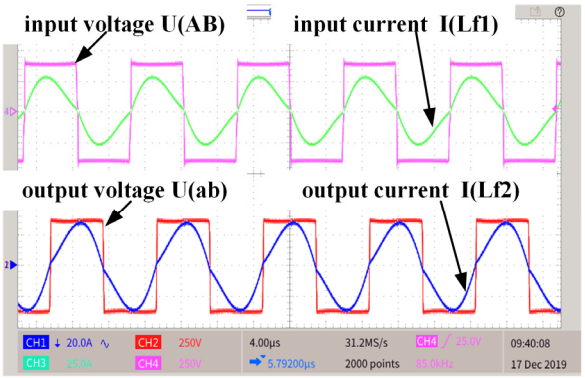

(a)

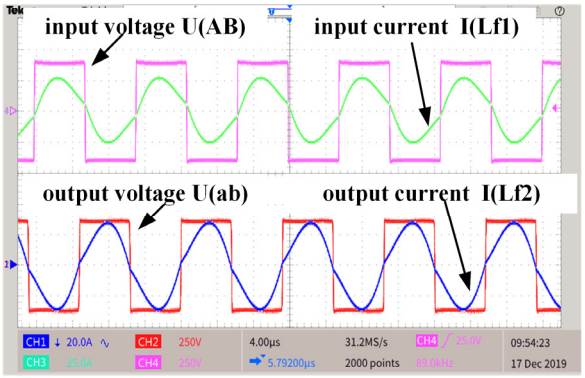

(b)

Fig. 16. Experiment waveform of $\mathbf{U}_{AB}$, $\mathbf{I}_{Lf1}$, $\mathbf{U}_{ab}$, $\mathbf{I}_{Lf2}$ (a) k=0.3, f=85kHz (b) k=0.15, f=89kHz.

changed for a higher output power. These acts together have the system works in a specific detuned state. Therefore, the input impedance of the system has been changed, and the phase difference between input and output voltages is no longer 90°.

It can be seen that the current of the MOSFET at the turn-off moment in Fig.16(b) is larger, which is to ensure the implementation of the soft switching. Compared with Fig.14, the results agree well with the simulation.

Fig.17 shows the efficiency screenshot at the output power of 6.6kW, Udc1 and Idc1 are input dc voltage and current, Udc2 and Idc2 are output dc voltage and current. P1 and P2 are input and output power, η represents the efficiency from the dc power

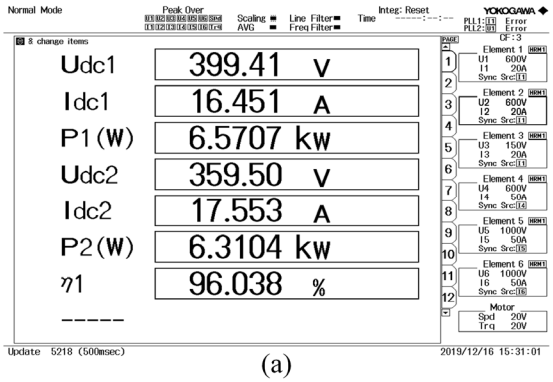

(a)

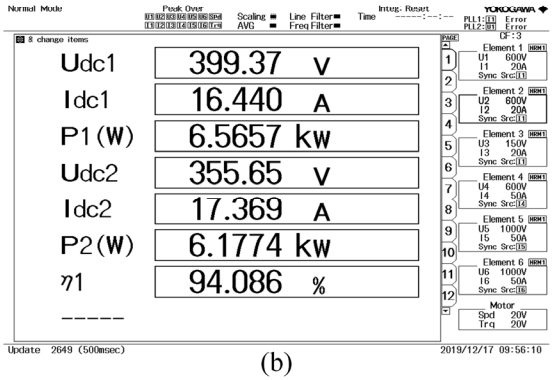

(b)

Fig. 17. Capture of efficiency from power meter at (a) k=0.3, f=85kHz (b) k=0.15, f=89kHz

supply to the resistive load. It can be observed that the transfer power reaches the target value of 6.17 kW even under worst-case coupling conditions. Moreover, due to the circuit detuning, an increase in conduction loss is inevitable, resulting in a slight reduction in efficiency, from 96% to 94%.

VI. Conclusion

Frequency tuning characteristics of three commonly used IPT compensation topologies, including SS, LCC-S, and LCC-LCC have been explored. Analytical expressions of the output power relating to the frequency, coupling coefficient, and other parameters are derived. It is found that the higher-order the compensation topology is, the more regular output power characteristic is obtained under the same coupler benchmark. To avoid the over-design of high order compensation parameter in coping with the wide coupling variation, the sensitivity analysis is carried out to find the parameters which have the greatest impact on the system. It is shown that tuning the value of pivotal compensation components for a detuned state is a viable way to maintain rated power even at the worst coupling condition. Simulation and experiments are implemented to validate the proposed method. A 6.6 kW prototype is built and proves that 6.1 kW can be transited with an efficiency of 94% when the coupling coefficient drops to half of its rated value. The parameter tuning strategy proposed in this paper can provide a reference for the related design of anti-misalignment applications.

This is the author accepted version of an article published in IEEE Journal of Emerging and Selected Topics in Power Electronics
https://doi.org/10.1109/JESTPE.2021.3077459

REFERENCES

[1] J. P. W. Chow, N. Chen, H. S. H. Chung and L. L. H. Chan, "An Investigation Into the Use of Orthogonal Winding in Loosely Coupled Link for Improving Power Transfer Efficiency Under Coil Misalignment," in IEEE Transactions on Power Electronics, vol. 30, no. 10, pp. 5632-5649, Oct. 2015.

[2] S. Hong, S. Jeong, S. Lee, B. Sim, H. Kim and J. Kim, "A Dual Resonance Near Field Communication Coil for EMF Reduction in Near Field Communication and Wireless Power Transfer Dual Coil System," 2019 IEEE International Symposium on Electromagnetic Compatibility, Signal & Power Integrity (EMC+SIPI), New Orleans, LA, USA, 2019, pp. 644-647.

[3] Y. D. Chung and J. S. Kim, "Improved efficiency characteristics of wireless power charging system for superconducting MAGLEV train using inserted permanent magnets," 2018 IEEE International Symposium on Electromagnetic Compatibility and 2018 IEEE Asia-Pacific Symposium on Electromagnetic Compatibility (EMC/APEMC), Singapore, 2018, pp. 564-567.

[4] S.Li and C. C. Mi, "Wireless power transfer for electric vehicle applications," IEEE J. Emerg. Sel. Topics Power Electron., vol. 3, no. 1, pp. 4–17,Mar. 2015.

[5] D. Patil, M. K. McDonough, J. M. Miller, B. Fahimi and P. T. Balsara, "Wireless Power Transfer for Vehicular Applications: Overview and Challenges," in IEEE Transactions on Transportation Electrification, vol. 4, no. 1, pp. 3-37, March 2018.

[6] N. A. Khan, H. Matsumoto and O. Trescases, "Wireless Electric Vehicle Charger with Electromagnetic Coil Based Position Correction using Impedance and Resonant Frequency Detection," DOI 10.1109/TPEL.2020.2965476 in IEEE Transactions on Power Electronics.

[7] J. P. K. Sampath, A. Alphones and D. M. Vilathgamuwa, "Figure of Merit for the Optimization of Wireless Power Transfer System Against Misalignment Tolerance," in IEEE Transactions on Power Electronics, vol. 32, no. 6, pp. 4359-4369, June 2017.

[8] A. Zaheer, H. Hao, G. A. Covic, and D. Kacprzak, "Investigation of multiple decoupled coil primary pad topologies in lumped IPT systems for interoperable electric vehicle charging," IEEE Trans. Power Electron., vol. 30, no. 4, pp. 1937–1955, Apr. 2015.

[9] S. Kim, G. A. Covic, and J. T. Boys, "Tripolar pad for inductive power transfer systems for EV charging," IEEE Trans. Power Electron., vol. 32, no. 7, pp. 5045–5057, Jul. 2017.

[10] F. Liu, Y. Yang, D. Jiang, X. Ruan and X. Chen, "Modeling and Optimization of Magnetically Coupled Resonant Wireless Power Transfer System With Varying Spatial Scales," in IEEE Transactions on Power Electronics, vol. 32, no. 4, pp. 3240-3250, April 2017.

[11] S. Y. Choi, J. Huh, W. Y. Lee and C. T. Rim, "Asymmetric Coil Sets for Wireless Stationary EV Chargers With Large Lateral Tolerance by Dominant Field Analysis," in IEEE Transactions on Power Electronics, vol. 29, no. 12, pp. 6406-6420, Dec. 2014.

[12] G. Ke, Q. Chen, W. Gao, S. Wong, C. K. Tse and Z. Zhang, "Research on IPT Resonant Converters With High Misalignment Tolerance Using Multicoil Receiver Set," in IEEE Transactions on Power Electronics, vol. 35, no. 4, pp. 3697-3712, April 2020.

[13] J. P. W. Chow, N. Chen, H. S. H. Chung and L. L. H. Chan, "An Investigation Into the Use of Orthogonal Winding in Loosely Coupled Link for Improving Power Transfer Efficiency Under Coil Misalignment," in IEEE Transactions on Power Electronics, vol. 30, no. 10, pp. 5632-5649, Oct. 2015.

[14] F. Liu, Z. Ding, X. Fu and R. M. Kennel, "Parametric Optimization of a Three-Phase MCR WPT System With Cylinder-Shaped Coils Oriented by Soft-Switching Range and Stable Output Power," in IEEE Transactions on Power Electronics, vol. 35, no. 1, pp. 1036-1044, Jan. 2020.

[15] Y. Zhang, T. Kan, Z. Yan and C. C. Mi, "Frequency and Voltage Tuning of Series–Series Compensated Wireless Power Transfer System to Sustain Rated Power Under Various Conditions," in IEEE Journal of Emerging and Selected Topics in Power Electronics, vol. 7, no. 2, pp. 1311-1317, June 2019.

[16] F. Lu, H. Hofmann, J. Deng and C. Mi, "Output power and efficiency sensitivity to circuit parameter variations in double-sided LCC-compensated wireless power transfer system," 2015 IEEE APEC, Charlotte, NC, pp. 597-601, 2015.

[17] K. Lu et al., "A Novel Efficiency-oriented Frequency Tracking Method for WPT Systems," 2019 22nd International Conference on Electrical Machines and Systems (ICEMS), Harbin, China, 2019, pp. 1-5, doi: 10.1109/ICEMS.2019.8921703.

[18] S. Liu, Y. Shen, Y. Wu, J. Lin and M. Hu, "Study on frequency tracking for wireless power transfer system using magnetic resonant coupling," 2018 13th IEEE Conference on Industrial Electronics and Applications (ICIEA), Wuhan, 2018, pp. 2569-2572, doi: 10.1109/ICIEA.2018.8398144.

[19] Wireless Power Transfer for Light-Duty Plug-In/Electric Vehicles and Alignment Methodology, Standard SAEJ2954, May 2016. [Online]. Available: http://standards.sae.org/j2954_201605/

[20] L. Zhao, D. J. Thrimawithana, U. K. Madawala, A. P. Hu and C. C. Mi, "A Misalignment-Tolerant Series-Hybrid Wireless EV Charging System With Integrated Magnetics," in IEEE Transactions on Power Electronics, vol. 34, no. 2, pp. 1276-1285, Feb. 2019.

[21] Feng H, Cai T , Duan S , et al. A Dual-Side Detuned Series-Series Compensated Resonant Converter for Wide Charging Region in Wireless Power Transfer System[J]. IEEE Transactions on Industrial Electronics, 2017:1-1.

[22] J. Yang, C. Jiao, X. Zhang, X. Yang and K. Zhang, "Design of an LCC-SP Compensated WPT System and Parameters Tuning Method for Misalignment Condition," 2020 4th International Conference on HVDC (HVDC), Xi'an, China, 2020, pp. 145-150, doi: 10.1109/HVDC50696.2020.9292889.

[23] Deng J , Li W , Nguyen T D , et al. Compact and Efficient Bipolar Coupler for Wireless Power Chargers: Design and Analysis[J]. IEEE Transactions on Power Electronics, 2015, 30(11):6130-6140.

[24] Y. Wang, H. Wang, T. Liang, X. Zhang, D. Xu and L. Cai, "Analysis and design of an LCC/S compensated resonant converter for inductively coupled power transfer," 2017 IEEE Transportation Electrification Conference and Expo, Asia-Pacific (ITEC Asia-Pacific), Harbin, 2017, pp. 1-5, doi: 10.1109/ITEC-AP.2017.8080829.

[25] S. Li, W. Li, J. Deng, T. D. Nguyen and C. C. Mi, "A Double-Sided LCC Compensation Network and Its Tuning Method for Wireless Power Transfer," in IEEE Transactions on Vehicular Technology, vol. 64, no. 6, pp. 2261-2273, June 2015, doi: 10.1109/TVT.2014.2347006.

[26] Swain A K , Devarakonda S , Madawala U K . Modeling, Sensitivity Analysis, and Controller Synthesis of Multipickup Bidirectional Inductive Power Transfer Systems[J]. IEEE Transactions on Industrial Informatics, 2014, 10(2):1372-1380.

[27] J. Lu, G. Zhu, H. Wang, F. Lu, J. Jiang and C. C. Mi, "Sensitivity Analysis of Inductive Power Transfer Systems With Voltage-Fed Compensation Topologies," in IEEE Transactions on Vehicular Technology, vol. 68, no. 5, pp. 4502-4513, May 2019.

Junjun Deng received the B.S., M.S., and Ph.D. degrees in electrical engineering from Northwestern Polytechnical University, Xi'an, China, in 2008, 2011, and 2015, respectively. From 2011 to 2014, he was a Visiting Scholar with the Department of Electrical and Computer Engineer, University of Michigan, Dearborn. In 2016, he has joined the Faculty of Vehicle Engineering, Beijing Institute of Technology, Beijing, China. His research interests include wireless power transfer, resonant power conversion, and electric motor drive for electric vehicles.

Qianning Mao was born in Shanxi,China, in 1996. She received the B.S. degree in vehicle engineering from Dalian University of Technology, Dalian, China, in 2018. She is currently pursuing the M.S degree in mechanical engineering with the National Engineering Laboratory for Electric Vehicles, at Beijing Institute of Technology, Beijing, China. Her main research interests include wireless power transfer.

This is the author accepted version of an article published in IEEE Journal of Emerging and Selected Topics in Power Electronics
https://doi.org/10.1109/JESTPE.2021.3077459

Wenbo Wang was born in Jiangxi, China, in 1996. He received the B.S degree in automotive engineering from Hunan University, Hunan, China, in 2018. He is currently working toward the Ph.D degree in mechanical engineering with the National Engineering Laboratory for Electric Vehicles, at Beijing Institute of Technology. His research interests include inductive power transfer and resonant converters.

Lantian Li received the B.S. degree in mechanical engineering from Beijing Institute of Technology, Beijing, China, in 2017. He is studying for a Ph.D. degree in mechanical engineering in the National Engineering Laboratory for Electric Vehicles from Beijing Institute of Technology, China and the Collaborative Innovation Center of Electric Vehicles in Beijing, China. He became a Student Member of IEEE in 2021. His main research interests are in the area of wireless power transfer.

Zhenpo Wang (Member, IEEE) received the Ph.D. degree in automotive engineering from the Beijing Institute of Technology, Beijing, China, in 2005.

He is currently a Professor with the School of Mechanical Engineering and the Director of the National Engineering Laboratory for Electric Vehicles, Beijing Institute of Technology. He has authored or coauthored four monographs and translated books and more than 80 technical articles. He also holds more than 60 patents. His current research interests include pure electric vehicle integration, packaging and energy management of battery systems, and charging station design.

Dr. Wang was a recipient of numerous awards, including the Second National Prize for Progress in Science and Technology, the First Prize for Progress in Science and Technology from the Ministry of Education, China, and the Second Prize for Progress in Science and Technology from the Beijing Municipal, China.

Shuo Wang received B.S. and M.S. degrees in electrical engineering from Shandong University of Science and Technology, and China University of Mining and Technology, Beijing, China in 2009 and 2012, respectively, and Ph.D degree in engineering from the faculty of engineering and information technology (FEIT), University of Technology, Sydney, NSW, Australia in 2017.

He is currently a Postdoctoral Research Fellow with the National Engineering Laboratory for Electric Vehicle at Beijing Institute of Technology from 2017. His research interests include electric vehicle charging technology, and the big data analysis for electric vehicle.

Giuseppe Guidi (M'00, SM'20) received the graduate degree from the University of L'Aquila, L'Aquila, Italy, in 1995, and the Ph.D. degree from the Norwegian University of Science and Technology (NTNU), Trondheim, Norway, in 2009. He has worked in the field of power electronics and industrial drives from 1997 to 2004, joining first Fuji Electric R&D, Japan, as R&D Engineer and then SIEI SpA, Italy, as a Senior Engineer. In 2009, he joined Yokohama National University, Yokohama, Japan, as a Research Associate, working on power converters for electric vehicles. From 2011 he was a part-time Research Associate with NTNU, until joining SINTEF Energy Research, Trondheim, Norway, in 2013. His current research interests include high power WPT systems for automotive and marine applications, drive systems for electric propulsion, as well as application of power electronics to renewable energy systems.

This is the author accepted version of an article published in IEEE Journal of Emerging and Selected Topics in Power Electronics
https://doi.org/10.1109/JESTPE.2021.3077459